ELSEVIER

Tectonophysics 355 (2002) 227–246

TECTONOPHYSICS

www.elsevier.com/locate/tecto

Multimode migration of scattered and converted waves for the structure of the Hikurangi slab interface, New Zealand

John N. Louie [a,*], Sergio Chávez-Pérez [b], Stuart Henrys [c], Stephen Bannister [c]

[a] *Seismological Laboratory and Department of Geological Sciences, Mackay School of Mines, The University of Nevada, Reno, NV 89557-0141, USA*

[b] *Direccion Ejecutiva de Exploracion y Produccion, Instituto Mexicano del Petroleo, Eje Central Lazaro Cardenas 152, Mexico DF 07730, Mexico*

[c] *Institute of Geological and Nuclear Sciences, 69 Gracefield Road, PO Box 30-368, Lower Hutt, New Zealand*

Received 27 November 2000; received in revised form 25 June 2001; accepted 8 August 2001

Abstract

Reflectivity imaging of local earthquake seismograms has revealed the structure of the Hikurangi subduction interface at the location of two strong earthquakes that occurred in 1990. The earthquakes originated within the continental plate of the North Island of New Zealand and below in the subducting Pacific slab. We used seismograms from 500 well-located events in two earthquake sequences recorded by a small temporary seismograph deployment to directly image the structure and multiphase reflectivity of the plate interface. Synthetic tests of the imaging method show the effects of the poor 3-d geometric coverage afforded by the seismometer array. Kirchhoff summation image sections computed from synthetics show accurate depth imaging of backscattering interfaces. Phase-converting interfaces imaged with forward-scattered waves are smeared by poor ray coverage to 5-km depth inaccuracy and are only imaged over a small range of their horizontal extent. From the data, we computed image sections for P–P, P–S, S–P and S–S scattering. We mitigated imaging artifacts due to poor ray coverage with an obliquity factor, an antialiasing criterion and enhancement by resampling statistics. Imaging used a sharply layered velocity model. We tested for the effects of imaging with first-arriving headwaves by imaging through smoothly varying velocity models. For our ray geometry, early-arrival headwaves contribute little to the images. The plate interface appears as a 3–5-km thick P–P and possibly S–S backscatterer with 5° NW dip, offset 5 km down-to-the-NW above a normal fault in the slab. When illuminated from below, a wedge of the interface on the downdip side of the slab fault forms a very prominent P–P forward scatterer. The edges of the wedge forward-scatter some S–P and S–S energy, but an order of magnitude less than the P–P forward scattering. The imbalances between forward scattering of P and S energy suggest a wedge of subducted sediment retaining significant porosity but with rigidity close to that of surrounding rocks.

Keywords: Subduction; Seismic reflection; Migration; Imaging; Shear wave; Thrust fault

1. Introduction

Here we show prestack migration reflectivity imaging using earthquake seismograms of subduction zone structure that hints at physical properties. We produce, for the first time, a detailed 3-d seismic scattering

* Corresponding author. Tel.: +1-775-784-4219.
E-mail address: louie@seismo.unr.edu (J.N. Louie).
URL: http://www.seismo.unr.edu.

0040-1951/02/$ - see front matter © 2002 Elsevier Science B.V. All rights reserved.
PII: S0040-1951(02)00144-0

image of a subduction interface that is operating in an accretionary mode. The prestack migration at the heart of our imaging procedure relies on simple acoustic assumptions that allow an approximate inverse to the elastic single-scattering problem by backprojection. The migration is almost identical to the procedures used in the petroleum industry to determine structural geometries from the phase information in the wavefield. Starting with the early P- and S-wave codas generated by swarms of earthquakes and recorded by local seismograph arrays, we employ this migration process to image complicated seismic arrivals into candidate reflective structures. By tuning this reflectivity imaging process to match P–P or S–S scattering, and S–P or P–S scattering with mode conversion, we obtain some information about the elastic properties of the structures.

Seismologists may be reluctant to believe that one can successfully image crustal faults using mainly P–P, isotropic scattering characteristics and earthquake sources. For instance, Aki (1992) shows that P–S conversion for seismic waves is much greater than S–P. Thus, the dominance of S waves in the coda of seismograms raises concern about the validity of dealing with only P–P scattering in imaging crustal reflectors. But oil-related seismic exploration sources are also rich in shear-wave energy, particularly surface sources such as vibrator arrays from which more than 86% of the seismic radiation must be shear waves (Tan, 1985). In spite of this dominance of shear-wave energy, successful P–P scattering applications abound in seismic imaging for fracture detection and reservoir characterization (e.g., Mittet et al., 1997). Chávez-Pérez and Louie (1998) showed the application of P–P scattering to crustal targets in southern California through wide-angle prestack migration of earthquake recordings.

We examine a west-directed, northwest-dipping subduction zone on the Hikurangi margin at the 1990 Weber earthquake sequence on the southeast margin of New Zealand's North Island (Fig. 1). The Hikurangi oceanic plateau on the Pacific tectonic plate subducts westward at the offshore Hikurangi Trough at 4–5 cm/year (DeMets et al., 1994) below the New Zealand continental fragment on the Australian plate. The Hikurangi is the southernmost end of the Tonga–Kermadec subduction zone.

The Weber events occurred midway between the earthquake sequences studied by Bannister (1988) to the north and by Robinson (1986) to the south. Davey et al. (1986) imaged the plate interface offshore from Cape Turnagain with a marine reflection survey showing a very shallow dip of 2–5°. Davey and Stern (1990) could trace interface reflections to 14-km depth in prestack migrations of this survey just offshore. The Hikurangi interface was previously examined to the northeast at East Cape (the Raukumara peninsula, Fig. 1) recently by Eberhart-Phillips and Reyners (1999), who found a 1–2-km thick plate interface with a high Vp/Vs ratio of 2 from S–P converted waves. Data for our reflectivity imaging of the subduction interface arises with the 500 "passive" sources of the Weber I and II intraplate earthquake sequences (Fig. 1).

1.1. The 1990 Weber earthquake sequences

The first Weber event was the M6.2 Weber I in February 1990, on a steep NW-dipping normal fault in the slab below the 20-km deep plate interface. That was followed 3 months later by the M6.4 Weber II event, which was a shallow-dipping southeast-directed thrust above the plate interface. Neither Weber sequence actually ruptured the plate interface at 20-km depth (Robinson, 1994). The Weber I event and its aftershocks are all northeast-striking normal mechanism events between 20- and 35-km depth within the downgoing oceanic Pacific plate. The Weber II event and its aftershocks 3 months later are all oblique east-directed thrusts on a northeast-striking fault, between 7- and 20-km depth within the overriding continental Australian plate.

Earthquake depths in the subducting lower plate show the Hikurangi is an extremely shallow subduction zone, dipping only 4° for up to 200 km west of the plate boundary where it then dives sharply below 20-km depth (Reyners, 1980; Robinson, 1986; Bannister, 1988). Seismic surveys (Davey et al., 1986, 1997; Davey and Smith, 1983; Davey and Stern, 1990) have confirmed the shallow depths and dip offshore, and suggested that the subducting Pacific plate is anomalously buoyant with 15-km crustal thickness. East of the Weber earthquake area, the offshore Pacific plate is layered with up to 2.5 km of sediment and interrupted by volcanic seamounts. As in the Cascadia subduction zone (Flueh et al., 1998), the buoyant and shallow-dipping slab accretes almost all of its thick sedimen-

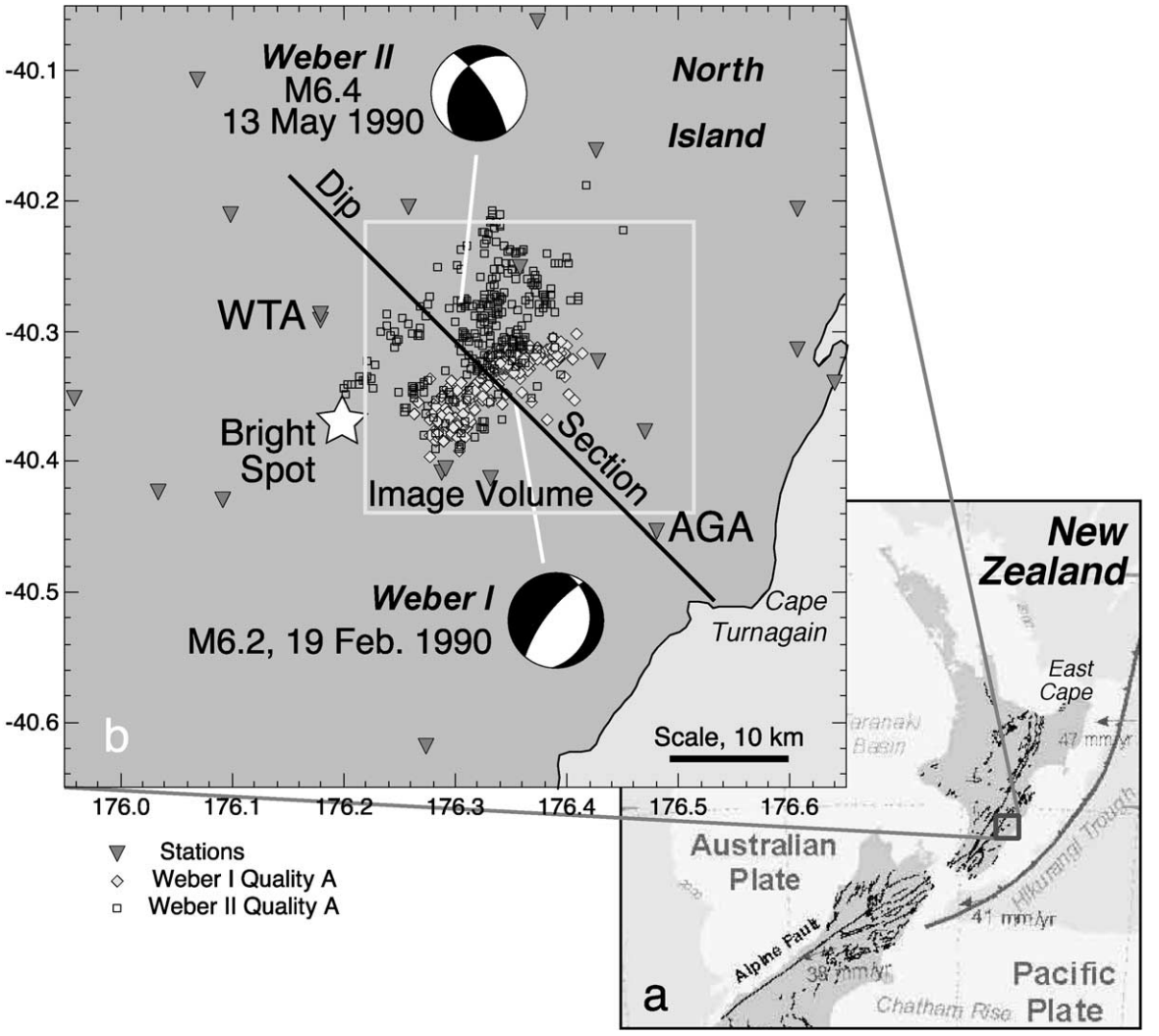

Fig. 1. Map of the Weber I and II earthquake sequences, with Robinson's (1994) lower-hemisphere focal mechanisms for the mainshocks. All the Weber I aftershocks (diamonds) were located below the 20-km deep plate interface, illuminating it from below with forward-scattered seismic energy. The Weber II event and all but a few of its aftershocks (squares) were above the interface, illuminating it from above with backscattered energy. Robinson's (1994) deployment of 10 portable seismometers (triangles with two stations noted) along with nearby permanent seismometers of the New Zealand Network provide the vertical-component seismograms we used for reflectivity imaging. Figs. 5, 7 and 8 show imaged seismic reflectivity cross sections along the NW–SE black line and Fig. 9 shows reflectivity volumes below the area outlined by the light square.

tary cover to the leading edge of the upper plate (Davey et al., 1986; Davey and Stern, 1990). We examine the properties of the subduction interface where it is buried at 20-km depth at the Weber events, about 150 km inland of the Hikurangi Trough (Fig. 1).

We are locating structures by seismic imaging, not by locating aftershock hypocenters. Robinson (1994) developed a local 1-d velocity model from recordings of the Weber earthquake sequence in this area during 1990 on a temporary local array of 10 seismometers. He relocated the events, showing that all aftershocks occurred on the rupture planes of their respective Weber I, II, III or IV main shocks. We are using these events as sources of energy to illuminate other struc-

tures, away from the ruptured faults. We examine both forward- and backscattering of this illumination. The Weber I sequence in the lower plate illuminates with forward-scattered energy the structures associated with the Weber II sequence in the upper plate, which occurred 3 months later. Conversely, the Weber II sequence illuminates with backscattered energy the deeper structures of the Weber I sequence months after their main period of activity.

A reflection imaging technique has resolution only where we have an array of both sources and receivers. For a receiver array, we have the New Zealand national network, mostly more than 100 km from Weber, supplemented by Robinson's (1994) 10-station portable deployment in 1990. For a source array, we use the 500 events with quality-A relocations by Robinson (1994). We used all recordings of the 500 quality-A events where the seismograph and the image point were separated by horizontal distances less than 70 km.

About 200 of the events are Weber I aftershocks in the lower plate; the rest are the Weber II event and its aftershocks in the upper plate. Robinson (1994) found that the data could determine a 1-d velocity model quite well, but did not contain 3-d velocity constraints. He also showed that composite mechanisms of each sequence were very similar to the mechanisms of the mainshocks.

We use only the vertical receiver components, although three components are available. Fig. 2 shows the good-quality data from the gain-ranged portables and permanent stations. For this figure, the traces are sorted and arranged not by epicentral distance, but in order of two-way reflection travel time from a spot on the plate interface (Fig. 1). This ordering allows us to see backscattered coherent arrivals from structures near the interface. These arrivals are nearly parallel to the P–P scatter arrival time marked at the top of Fig. 2 for 123 Weber II aftershocks recorded at station

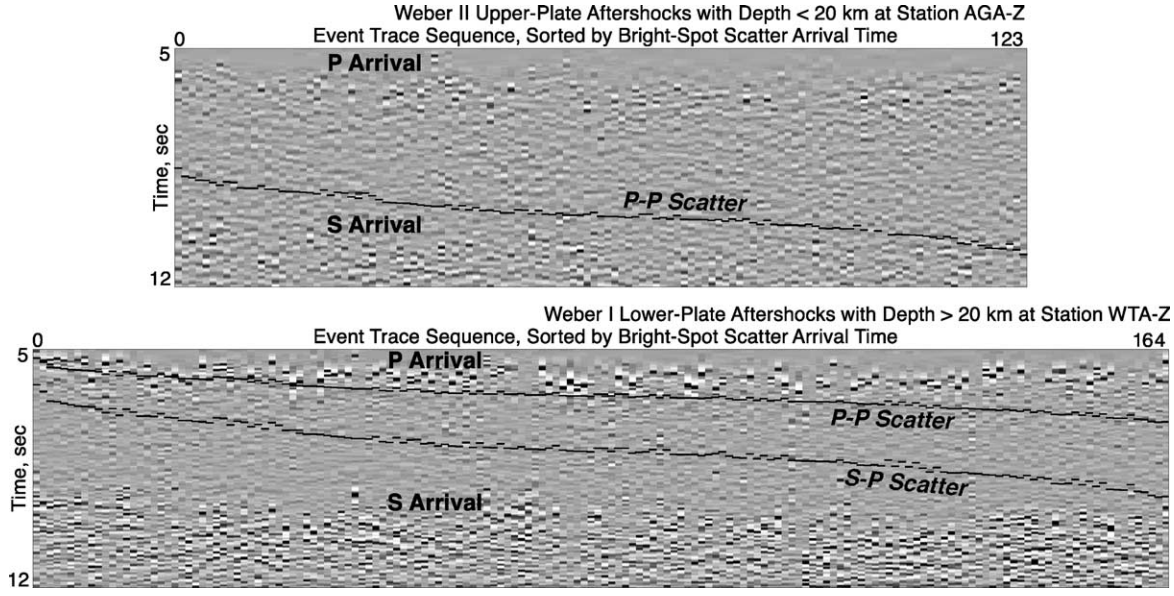

Fig. 2. Common-receiver record sections of 1990 recordings of Weber I (below) and II (above) aftershocks on stations WTA and AGA, respectively (Fig. 1). The 1-Hz vertical-component instruments in Robinson's (1994) portable deployment were gain-ranged to prevent digitizer saturation (clipping) and are plotted as variable-density vertical strips in the images after trace equalization. Event magnitudes ranged from 1.0 to 6.4. The traces have epicentral distances ranging from 5 to 30 km and event depths ranging from 7 to 39 km. The traces are arranged in order of diffraction travel times to the "bright spot" on the plate interface at 20-km depth (Fig. 1) and not by direct-wave arrival time or azimuth. Thus, reflections and conversions at the plate interface should be coherent from trace to trace while the direct arrivals appear broken. The black lines trace the arrival time across the sections of: top, P–P backscattering at the plate interface from the Weber II events in the upper plate; and bottom, P–P forward scattering and S–P conversion at the plate interface from the Weber I events in the lower plate. Note the direct S arrival has similar amplitude to, and does not stand out against, the earlier-arriving backscattered reflections and converted phases from the upper-plate event. The horizontal-component Weber II recordings share these emergent S arrivals.

AGA (Fig. 1). The imaging procedure itself identifies the coherent energy that fits the time imaging conditions of our migration.

Nowhere in the Weber data set do we see the strong S–P conversions that Eberhart-Phillips and Reyners (1999) and Bannister (1988) saw to the northeast. Such conversions would be obvious in the lower part of Fig. 2, parallel to the S–P scatter arrival times, if they were strong. This section presents 164 Weber I events below the interface recorded at station WTA (Fig. 1). The Hikurangi subduction interface usually produces prominent conversions of shear waves from events below it to P waves (Reyners, 1980; Robinson, 1986; Bannister, 1988; Eberhart-Phillips and Reyners, 1999). The phase conversions and low shear velocities (Reyners et al., 1999) suggest the interface to be unusually rich in sediment and fluid, at least in front of seamounts or other structures on the plate. Reyners (1980) had found strong S–P conversions from the plate interface near Weber decades before the 1990 earthquakes. The absence of such strong conversions at the interface (Fig. 2, lower) following the large intraplate Weber I normal-faulting earthquake in 1990 suggests the elastic properties of the plate interface may change substantially over time.

2. Methods

For structural imaging, we are interested first in acoustic images, equivalent to Lamé parameter lambda images. Our efforts to resolve structure are assisted by the special isotropic P–P scattering property for variations in P velocity. The strength of the P–P scattered waves we image depends on Lamé parameter lambda perturbations, which under asymptotic assumptions radiate like point explosions (Wu and Aki, 1985). Forward- and backscattered waves will have the same phase and amplitude. Without having to separate scattered phases on the basis of incidence angle or amplitude-versus-offset, we image variations in the Lamé parameter lambda due to its independence of reflection angle. This lambda variation imaging is as significant as impedance imaging, since it is proportional to the relationship between compressional and shear velocities (Sato, 1984; Le Bras, 1985; Louie, 1990; Ikelle et al., 1992; Chávez-Pérez and Louie, 1998).

Elastic synthetics illustrate the isotropic scattering property of Lamé lambda perturbations against the more intuitive scattering of rigidity perturbations. Fig. 3 shows vertical component elastic synthetics for two-layer models where Vp jumps with depth from 5 to 6 km/s while Vs stays at 2.9 km/s (for 131% lambda-only perturbation), or where Vs jumps as well to 3.7

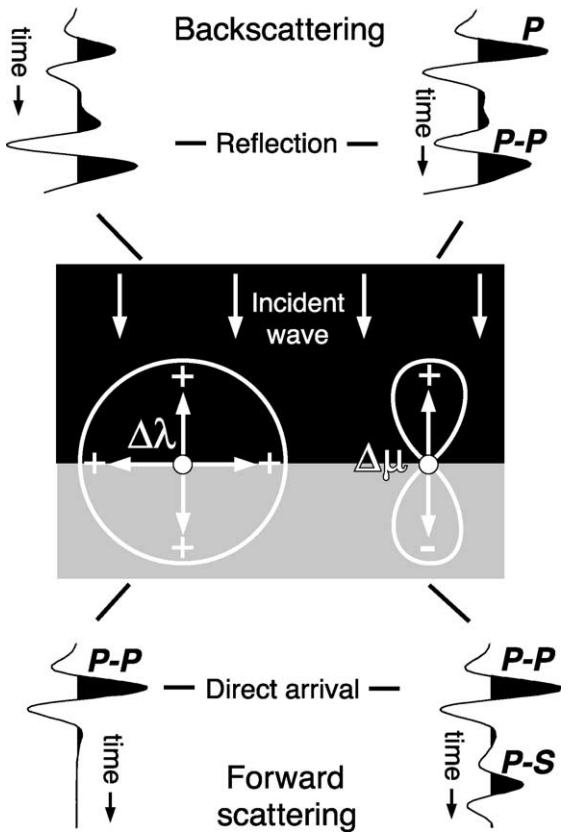

Fig. 3. Vertical-component elastic synthetics for a two-layer model showing the early P-wave coda for variations in Lamé parameters (λ and μ) during back- and forward-scattering. A point scatterer on the interface (left white dot) that is an asymptotic variation only in lambda ($\Delta\lambda$, corresponding to a P-velocity but not an S-velocity difference) will act as a point explosion when hit by a vertically incident wave, and radiate scattered waves of equal amplitude and sign in all directions (Wu and Aki, 1985). This isotropic scattering radiation is represented by the circular polar plot of constant reflection coefficient. A scatterer that is a variation in rigidity mu (right white dot) but not in lambda ($\Delta\mu$, which produces both P- and S-velocity differences) will act as a point couple, radiating as the cosine squared of the incidence angle, and represented by the sigmoid polar plot of reflection coefficient. Note the absence of a forward-scattered S wave for the lambda scattering component.

km/s (creating a 65% rigidity-only, or mu, perturbation). A fourth-order finite difference code (Levander, 1988) uses a vertical motion line source of an assumed Ricker wavelet with 2-Hz central frequency. For backscattered waves, the source is located at 5-km depth, whereas for forward-scattered waves the source is located at 15 km. All four seismograms are recorded on the surface at a (horizontal) source–receiver distance of 20.8 km. The interface is located at 10-km depth.

2.1. Lamé lambda, P velocity and isotropic scattering

The backscattering case (Fig. 3) shows the first arrival and the early "coda of reflection" (depicting a P–P reflection) for variations in Lamé parameters. The forward-scattering case shows the first arrival (depicting a P–P transmission) and the early "coda of transmission" after that. Note the absence of a forward-scattered S wave (i.e., there is no P–S energy conversion) for the lambda-only scattering component despite the nonnormal incidence of energy.

The contributions of lambda variations are isotropic (Wu and Aki, 1985) and come from local P wave energy, mostly P–P reflections and transmitted P-wave arrivals (Fig. 3). This is clearly not the case when one tries to obtain density images or rigidity images. For instance, rigidity (mu) variations lead to anisotropic scattering and one needs to take S waves into account (Fig. 3) to correctly image such variations. In the presence of lambda variations, both back- and forward-scattered events can constructively interfere upon migration, while for a rigidity variation they tend to cancel out. The search for structure with lambda (or P-velocity) variations requires only the use of P waves, whereas the search for rigidity variations requires the use of P and S waves. Thus, the search for structures on the basis of P-velocity variations becomes practical with an acoustic processing scheme.

2.2. Prestack multimode depth migration

The depth migration method we use is a backprojection of assumed primary reflection amplitudes into a depth section based on travel times through an assumed velocity model. The backprojection requires knowledge of the source wavelet for deconvolution by cross-correlation with each seismic trace (Louie et al., 1988; Le Bras and Clayton, 1988). Chávez-Pérez and Louie (1998) roughly approximated this by cross-correlating with a boxcar function 0.5 s long, close to the central period of the expected reflection arrivals. The net effect of boxcar correlation is to smooth the migration (through low-pass filtering of the data), center the reflection pulses near zero phase, and avoid operator aliasing.

We now set the length of the cross-correlated boxcar "on the fly" with the operator antialiasing criterion of Lumley et al. (1994). This criterion tends to favor reflectors that have low dip, when observed at smaller source–receiver distances, or offsets. Bandpass filtering of the data before migration, keeping frequencies only between 1 and 8 Hz, prevents high frequencies in the near-offset traces from dominating the migrated images. Where the high-cut frequency required for antialiasing becomes too low, and the boxcar length becomes longer than about 20 s, a particular trace is not summed into the migration. To avoid producing a laterally discontinuous image holding only scattered near-horizontal reflectors, we relax the antialiasing criterion by applying apparent source and receiver spacings (Lumley et al., 1994) that are closer to the minimum than to the maximum of the true spacings.

The antialiasing filtering also minimizes phase differences arising from our lack of account for focal mechanisms. We image using travel times computed through one-dimensional velocity models, ignoring lateral velocity variations. Our Kirchhoff prestack depth migration process is similar to that of Louie et al. (1988). The migration backprojects assumed primary reflection amplitudes into a depth section. It has been identified by Le Bras and Clayton (1988) as the tomographic inverse of the acoustic wave equation under the Born approximation in the far field, utilizing WKBJ rays for downward continuation and two-way reflection travel time for the imaging condition. Travel time versus distance matrices we compute from assumed velocity profiles using Vidale's (1988) finite difference solution to the eikonal equation. We obtain the final depth-imaged section by stacking the migrated partial images from individual events (common source records) or stations (common receiver records).

We achieve an approximate multimode migration by simply altering the travel times that form the process's imaging condition. As described by Louie

et al. (1988) and Chávez-Pérez and Louie (1998), the imaging condition for P–P reflections uses a P-wave travel time from the source to the candidate reflection point, plus a P-wave travel time from the reflection point to the receiver. For a multimode migration, we simply use the travel time of the desired mode on the appropriate part of the travel path. For the Weber sequence, Robinson (1994) did not determine a separate shear-velocity profile. Hence we roughly estimate the shear-wave travel time for a branch by multiplying its P-wave travel time by the square root of three. So, to compute the imaging condition for an S–P reflection image, for example, we add the shear-wave travel time from the source to the reflection point to the P-wave travel time from the reflection point to the receiver.

A multimode migration image must of course be constructed with reference to shear waves and the strong effects of rigidity perturbations on reflected amplitude and sign versus incidence angle (Fig. 3). Since we do not account for incidence angle, as Le Bras and Clayton (1988) describe in computing migrations for density variations, our multimode images will not reconstruct properly when summing forward- and backscattered data together. We address this problem only by keeping the migrations of forward- and backscattered seismograms separate. Such a strategy can only be effective where we are targeting one limited reflective area and can separate out sources from either side of it. The Hikurangi plate interface presents such a target, having sources from the Weber earthquake sequence in swarms both above and below it.

We also ignore source takeoff angle in this work and we do not correct for even the generally known source mechanisms of the earthquakes in the Weber sequence (Robinson, 1994). Again, the Weber sequence and the temporary seismometer array have a geometry that allows us to image the Hikurangi interface using on average the strong radiation from just one quadrant of the focal spheres. The images include data from aftershocks having nearly identical mechanisms and distributed over relatively small areas. We did not adjust the signs of seismograms according to picked P-wave first motions as Chávez-Pérez and Louie (1998) did. That procedure was most appropriate for strike-slip earthquakes.

We add a criterion that a seismogram cannot contribute to reflection points lying within 1-s travel time of the source (i.e., if the source branch image time is less than 1 s, no amplitude is summed into the image). This minimum-source-time criterion avoids canceling of multimode reflectivity near the focal sphere. As well, it conforms to the far-field assumptions in the migration theory put forward by Le Bras and Clayton (1988).

2.3. Artifacts and image enhancement

One of the major problems in Kirchhoff depth migration is image resolution. When we apply this method to data with limited observation geometry, artifacts or false images appear and make the results difficult to interpret. In this case, sparse receiver coverage causes artifacts along elliptical trajectories in the migrated depth section, spreading seismogram amplitudes out along surfaces of equal diffraction travel time. Defocusing of P–S and S–P converted energy by the P–P migration also contributes to image degradation (as would defocusing of P–P energy by an S–P migration). Strong noise will also produce upward sweeping artifacts in the form of "smiles" (i.e., lateral smearing of discontinuous reflections into synforms). Since at the Hikurangi plate interface, we are interested most in nearly horizontal structure, we apply the square of the standard obliquity factor in the migration. The extra factor of the cosine of the structural dip emphasizes horizontal structures in our images at the expense of near-vertical structures.

We apply trace equalization for receiver amplitude balancing and approximate spherical divergence correction (i.e., the amplitudes are normalized so that the mean-squared amplitude over the Pg–Sg part of the trace is the same for all traces). When the data are trace-equalized before stack, the effect of noisy traces on the stack is small and precise data editing is not crucial. This is useful for earthquakes because it is roughly equivalent to energy normalization for varying magnitudes and station responses. If noise were small, this procedure would lead to a perfect spherical divergence correction. However, we expect that there is more noise than signal. Thus, trace equalization boosts late arrivals in a practical manner, keeping the noise at the same level for all the traces.

To test the validity of our images, we must determine which imaged structures are real and which are artifacts produced from the imaging of noisy data. One test is a simple resampling analysis, which is

done by imaging the data after destroying trace-to-trace coherence by randomly flipping the signs of data traces. Images of resampled data allow us to observe mostly the problems with poor station distribution and coverage, the inadequate number of sources and the effects due to Kirchhoff operator aliasing. We can directly compare the image resulting from the resampling against the data image to note which features are likely to be artifacts.

Regarding the images migrated from resampled data as transformed noise estimates, we use the focusing measure of Harlan et al. (1984) to enhance the migrated images. This method makes a Bayesian estimate of the expected signal proportion at each image point, given the amplitude histograms of data and noise images (or transforms). We use the signal expectation image to weight or screen the data migration images. The weighting enhances those areas of the sections arising from the reflections with the most trace-to-trace coherency in the receiver data. The poorly sampled parts of the images containing mostly smeared, upward sweeping "smile" artifacts are screened out. Chávez-Pérez et al. (1998) show the application of this enhancement to prestack migration of shallow-crustal seismic reflection data.

2.4. Synthetic 3-d migration tests

For tests of 3-d Kirchhoff reconstruction below a sparse seismometer array, we use again a finite difference elastic modeling code (Levander, 1988) and the P–P migration procedure described in Chávez-Pérez and Louie (1998). This migration differs from the procedures described above mainly in that it uses no obliquity factor or minimum-source-time criterion. Line sources are the seismic excitation without conversion to point sources. For the tests, we used a more widely spread but much less dense seismometer distribution of over 100 stations, similar to that of the southern California Network (as shown in Chávez-Pérez and Louie, 1998) and not the 10-station Weber deployment of Robinson (1994). The geometry we used is one of the worst situations one would expect to find: a small number of sources at all crustal depths, and widely scattered receivers.

We tested the isotropic reflectivity imaging concept with a flat-layer model of isolated property variations (not shown). The contributions from individual events depicted reflectivity sign changes along the interfaces, where Kirchhoff trajectories—surfaces of equal reflection travel time—from different receivers at very different azimuths contribute to constructing the interface image. In addition, deep sources contribute sign changes along interfaces due to stretching along Kirchhoff trajectories of equal diffraction travel time. The polarity of a reflection from an interface between two very distinct media depends upon whether the incident wave arrives from above or below the interface; the amplitudes of all image points derived from a forward-scattered ray have to be multiplied by -1 before being added in. If this is not done, energy from sources above and below a reflector would tend to cancel instead of adding constructively (Zhiming et al., 1984). The exception is point Lamé parameter lambda diffractors, which have the same reflectivity for all directions of incidence (e.g., Hu et al., 1988; Zhu and Lines, 1997). We do not do a sign correction based on incidence because the migration algorithm treats the problem as a P–P scattering case for lots of lambda-variation isotropic point diffractors, having the same reflectivity for all directions of incidence. Note that we assume these diffractors are not between distinct media, but only small-scale asymptotic perturbations upon a smooth velocity background.

Fig. 4a shows a simple model testing our ability to image a low-velocity fault zone. It corresponds to the material properties of the fault zone model of Igel et al. (1997) used to simulate SH- and P–SV trapped-wave propagation in vertical strike-slip fault zones. However, we model here a flat-layered, low-velocity fault zone similar to a subduction interface. There are five sources with an assumed Ricker wavelet of 3 Hz central frequency, located above and below the low-velocity fault zones at depths of 3, 5, 6, 13, 14 and 15 km. The receiver configuration of the southern California Network (as shown in Chávez-Pérez and Louie, 1998) is used for this test. Fig. 4b and d shows the migrated images for the summation of all six contributions, with dip filtering (Hale and Claerbout, 1983) after migration. Fig. 4c and e shows the migrated images of synthetic data after resampling to destroy prestack trace-to-trace coherency.

Note how one can only image, in comparison to the resampled images, distorted pieces of the fault zones. This effect is due to reflectivity stretching along Kirchhoff trajectories of equal reflection travel time.

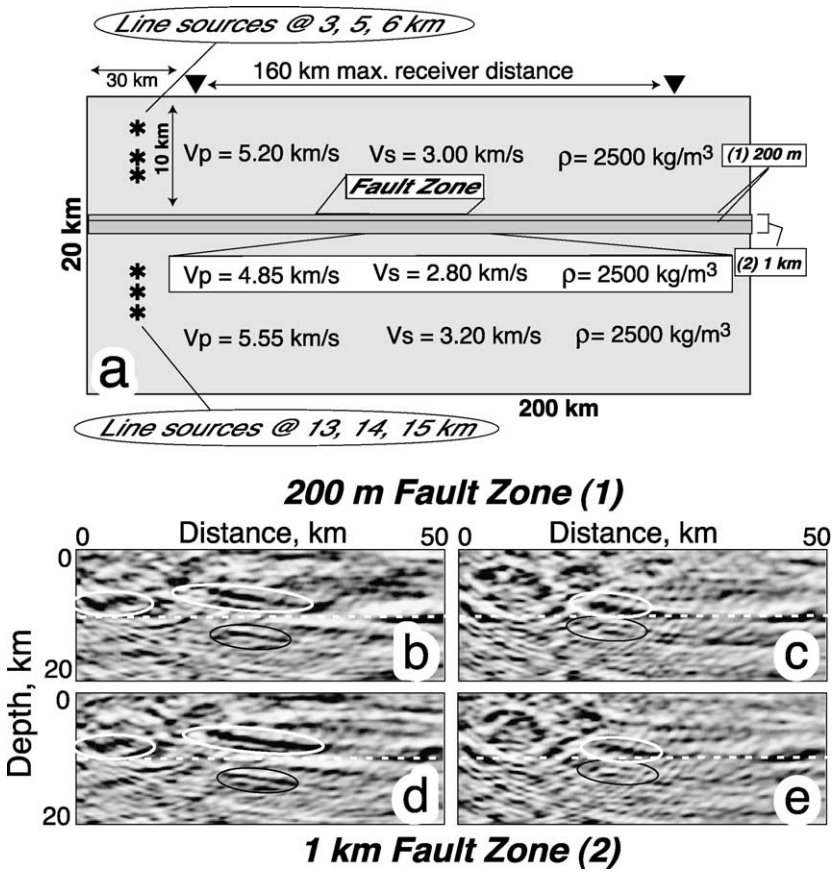

Fig. 4. (a) Velocity model and material properties for two horizontal low-velocity fault zone models at 10-km depth. Receivers (black inverted triangles) depict the distance range of model stations used. Fault zone (1) is a 200-m thick flat layer. Fault zone (2) is a 1-km thick flat layer. Six modeled sources at the depths given are summed into each migration. Below, migrated synthetics are on the left, and migrated resampled noise estimates are on the right. (b) Migrated depth section (dip filtered) for the 200-m fault zone (1). (c) Resampled migrated section (dip filtered) for the 200-m fault zone (1). (d) Migrated depth section (dip filtered) for the 1-km fault zone (2). (e) Resampled migrated section (dip filtered) for the 1-km fault zone (2). The white dashed line depicts the 10-km depth level where the upper interface of both fault zones is located. White ellipses show pieces of the imaged fault zones (b, d) and artifacts (c, e), whereas black ellipses show multiples (b, d) and artifacts (c, e).

Even in this synthetic example, the realistic sparse receiver distribution has left the fault-zone images at depths as much as one wavelength in error. Here, the depth error is about 2 km. Such errors prevent us from identifying the true phase of the imaged reflection or the sign of the reflection coefficient. This result is, however, very encouraging because of the very small thicknesses of the low velocity zones, less than the predominant seismic wavelength, and zones' perturbations of equivalent magnitude for both the Lamé parameters lambda and rigidity. The lambda image has to cut through the sign reversals that scramble the rigidity image.

2.5. Kirchhoff trajectories and reflection-point coverage

Given an arrival from a source at a station at a given time, we assume it diffracted from some point on an ellipsoid with the source and receiver as foci, a surface of constant diffraction travel time (Fig. 5). The ellipsoids are the Kirchhoff migration trajectories through the images. For the long cigar-like ellipsoids the backscattering occurs near the tip and butt of the cigar, with forward scattering occurring around the belly. Although we include here both forward- and backscattered waves, it takes many sources, many

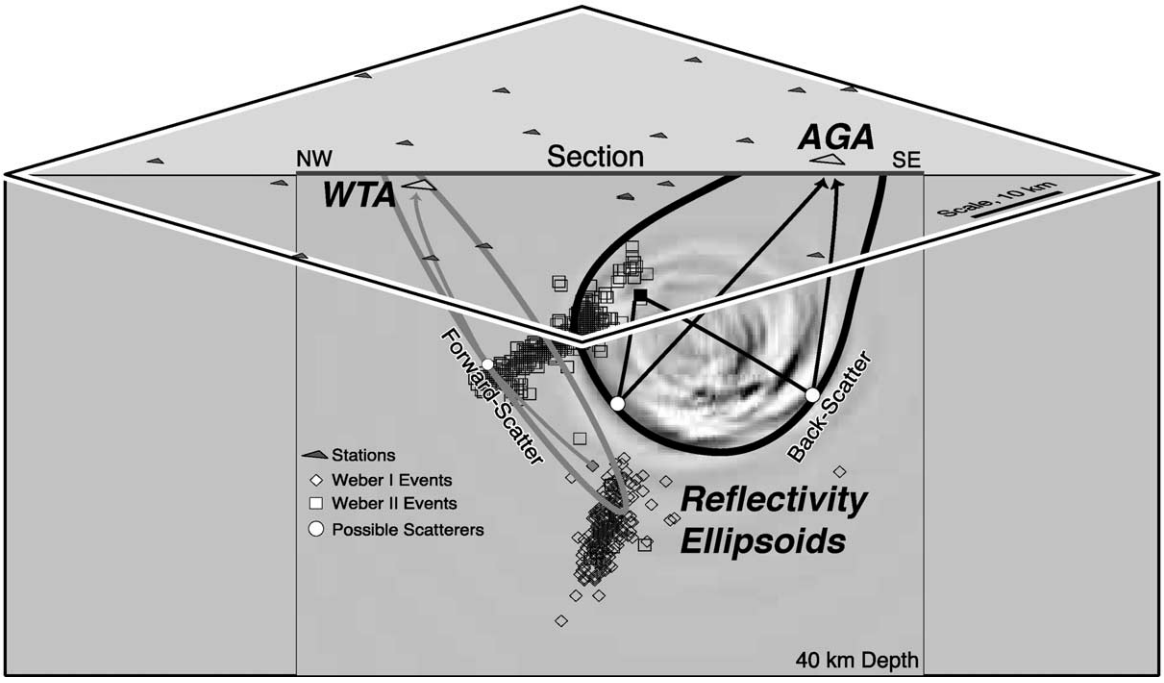

Fig. 5. A portion of the station map of Fig. 1, cut away to show a partial migration example in the 40-km deep section. Robinson's (1994) relocated hypocenters for the Weber I and II sequences are projected into the NW-striking section plane. The image example shows the migration of the Weber II recordings at station AGA from Fig. 2 (upper) into this section. White indicates negative migrated reflectivity, black positive reflectivity and gray little reflectivity. The black ellipsoid suggests a locus of backscattered reflection points with an event (black square) and station AGA (black arrows) as its foci. The elongated gray ellipsoid suggests a locus of forward-scattered reflection (or diffraction) points from a Weber I event below the 20-km deep slab interface, to station WTA (with data shown in Fig. 2, lower). Note that the forward-scatter travel time will be only slightly larger than the direct time (as in Fig. 2, lower) and that no ellipsoid foci are likely to be in any one section plane.

receivers and many ellipsoids to define a structure well. Thus, we can only image a limited volume between an event swarm and a receiver array, or below both (Von Seggern, 1994).

A 2-d migration of 2-d synthetic acoustic seismograms shows the resolution limits imposed by the limited source and receiver coverage. Fifty 2-d acoustic line sources were buried at depths of 15–20 km within Robinson's (1994) 1-d velocity model to generate a set of 500 synthetic seismograms with frequency centered around 6 Hz. Using all the procedures described above, the synthetics were migrated into the 2-d P–P reflectivity section shown in Fig. 6. This section would represent a region along the strike of the plate interface, centered near the star on Fig. 1. Since the synthetics were generated from a 1-d velocity model, the only reflections should be those from the flat interfaces in the model. For Fig. 6, the enhancement by Bayesian signal expectation (Harlan et al., 1984), minimum source time and squared obliquity were all applied.

Interfaces below the sources only focus in Fig. 6 where "depth point" coverage (the density of reflecting points at depth producing data at the receivers) is excellent, with incomplete source deconvolution resulting in about 2-km depth uncertainty. The focusing of overlying interfaces from forward-scattered waves is very poor. Only the presence of a scatterer is suggested, with more than 5-km placement uncertainty within the section. The image of a forward-scattering interface is stretched considerably above it, along the predominant ray paths.

This method provides a practical 3-d imaging tool that allows merging of forward- and backscattered P–P modes for structures having Lamé lambda variations. Additional modes of scattering (P–S, S–P and S–S) can be imaged if the forward- and backscattered

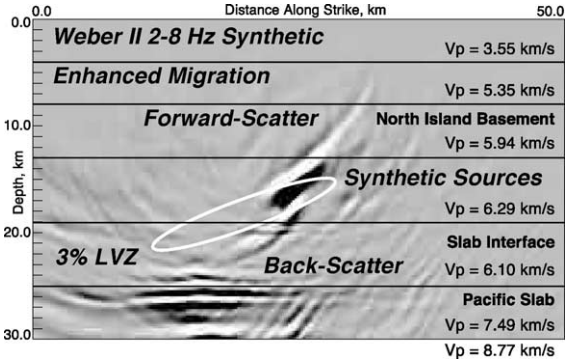

Fig. 6. Migration example of 2-d acoustic synthetic seismograms, created with the 1-d velocity model used by Robinson (1994) to relocate Weber events. The horizontal lines show the depths of the velocity interfaces in the model. The layers have the constant velocities indicated. The LVZ is the 3% velocity drop at the 20-km-deep slab interface. Fifty model sources within the tilted region outlined in white, crossing the interface, were propagated into 10 vertical-component model receivers on the surface. Processing of this resampling-enhanced migration was identical to processing of the Weber event data. White indicates negative reflectivity, black positive reflectivity and gray little reflectivity. The velocity increase at 26-km depth below the LVZ interface images strongly from backscattered reflections, but only directly below the sources. The top of the interface (LVZ) appears strongly as poorly-focused forward-scattered reflectivity above the interface, but only over a limited lateral extent of the interface.

data are migrated separately. Elliptical Kirchhoff trajectories and artifacts due to sparse station distribution appear in all images. However, most can be explained in terms of inadequate receiver coverage and incomplete summation. Two-dimensional acoustic synthetics and 2-d Kirchhoff migration make allowance for the reconstruction of dipping scattering structures. For the case of 2-d elastic synthetics and 3-d Kirchhoff migration, interface details and properties are obscured by phase changes, but structure is interpretable. A simple but effective resampling analysis allows identification of real structures against imaging artifacts. Resampling tests show migrated random noise will not mimic structures.

3. Results: multimode images of the plate interface

The eight dip sections in Fig. 7 separate out the multimode migration of P–P, P–S, S–P and S–S forward- and backscatterers from the Weber event data. Fig. 7a–d is mostly backscattered images using the shallow Weber II sources. Below in Fig. 7e–h are mostly forward-scattered images using the deep Weber I sources. Fig. 1 shows the line of section.

Superimposed are northeastward views into the focal spheres of the source mainshocks for each section. The refracted nodal plane of the Weber I events is clear between the white negative and black positive reflectivities in the forward-scattered P–P image of Fig. 7e. The focal spheres make it clear how we are imaging largely from a single quadrant of each mechanism.

Resolution is best for P–P backscatter below the Weber II sequence, illuminating the slab interface in some detail (Fig. 7a). These details are similar though not as clear in the S–S image (Fig. 7d). The P–S backscatter (Fig. 7b), using only arrivals between the P and S arrival, does not get enough data to focus well geometrically. Its Kirchhoff arcs nevertheless intersect prominent structures. The S–P backscatter image (Fig. 7c) can include more data, and shows the interface well over a small area. The P–P forward scattering (Fig. 7e) is especially strong, considering how much less P–S, S–P, or S–S forward scattering takes place. Forward scattering is strongest in a wedge above and just northwest of the Weber I sequence.

3.1. Structural interpretation

An interpretation of the reflectivity sections in Fig. 7 is not possible without reference to the extensive previous work on Hikurangi subduction. It is also necessary to refer to the synthetic images in Figs. 4 and 6 to understand how structures will appear in such sections. Most fundamental are the findings of Bannister (1988), Davey and Smith (1983), Davey and Stern (1990), Davey et al. (1997), Eberhart-Phillips and Reyners (1999), Reyners (1980), Reyners et al. (1999) and Robinson (1986, 1994): the slab interface is at 20-km depth in the Weber area; it dips about 5° northwest; the oceanic plate is greatly thickened by Chatham Rise and Hikurangi oceanic plateau basalts, seamounts, and sediments; is cut by normal faults; and a low-velocity zone 2–5 km thick is present along the plate interface. The interpreted structure is drawn on Fig. 7 beginning purely with these previous results.

We propose in Fig. 7 that the plate interface has been offset down to the northwest by 3–4 km. The

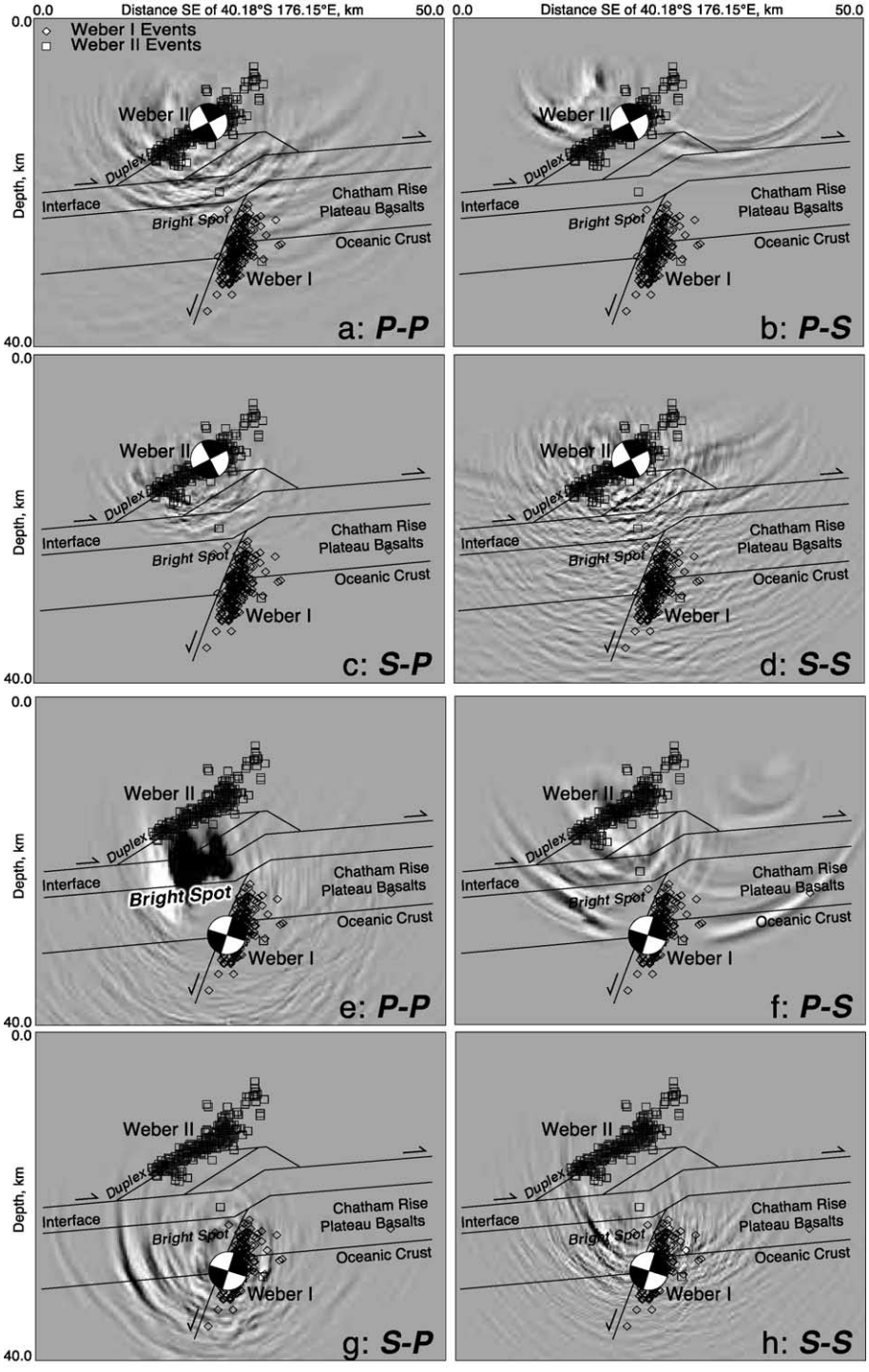
0.0
Distance SE of 40.18°S 176.15°E, km
50.0
Weber I Events
Weber II Events
Depth, km
40.0
Weber II
Duplex
Interface
Bright Spot
Chatham Rise
Plateau Basalts
Oceanic Crust
Weber I
a: P-P
b: P-S
c: S-P
d: S-S
e: P-P
f: P-S
g: S-P
h: S-S

synthetic tests of Fig. 4 allow us confidence that a very thin low-velocity zone can be imaged despite abundant interference from artifacts of poor geometric coverage. The test in Fig. 6 shows us that reflectors below the sources and imaged by backscattered waves will image, with the correct dip, at a depth within a few kilometers of the correct depth. Comparisons of resampled images of migrated noise against the data migrations also show us that the imaged reflector will only appear along the segment of the structure directly below the swarm of sources. At the edges, Kirchhoff artifacts will curve upwards. Chávez-Pérez et al. (1998) and Chávez-Pérez and Louie (1998) showed tests confirming that prestack Kirchhoff migration will maintain the true geometric relations between intersecting structures, even though absolute depths may have significant error.

We combine these observations on the performance of prestack migration to interpret slab-interface structure on the backscattered P–P image of Fig. 7a. In the center of the section at 17–23-km depth, directly under the swarm of Weber II events (small squares), our interpretation of the plate interface boundaries follows the coherent positive reflectivities (black tones in image). Where the interpreted structure reaches beyond the area under the Weber II swarm, our interpretation simply maintains the 5° dip known regionally rather than follow the migration artifacts upwards. The "bright spot" of strong P–P reflection, at 22.8-km depth under the Weber II swarm, follows the 5° regional dip exactly. Fig. 8d and e shows this section larger and without interpretation overlain.

The bright spot reflection is interrupted to the east, exactly where the shallowest Weber I normal-faulting events project in Robinson's (1994) relocation. This interruption is believable because it is still underneath the Weber II swarm, where there is sufficient geometric coverage. To find a reflection of similar strength east of the Weber I events but still below the Weber II swarm, we bend the interpreted base of the interface up 3–4 km in a ramp dipping NW at 30°. This displaced reflection can be followed for a few kilometers SE on Fig. 7a until it extends beyond the area under the Weber II swarm and is swept into an upward-bending artifact.

In drawing the 30° ramp in the bottom of the plate interface on Fig. 7a, we are proposing a ramp in the entire 3–5-km thick interface. At 5 km directly above the interpreted ramp is another 30° NW-dipping structure, which connects down to a 5° NW-dipping reflector immediately above the bright-spot reflector. Following both strong positive reflections (black tones) immediately above the bright spot, and both ramps 3–4 km up to the SE, gives us an interpretation of a bend or step in a low-velocity zone, with a double reflection following its upper and lower boundaries. All of this is defined directly below the Weber II event swarm where image quality will be best.

There is a 30° NW-dipping reflection between the two ramps defining the bend in the interface. It is certainly possible that this reflection represents the base of the interface and shows the interface thins over the ramp toward the SE. The interpretation drawn on Fig. 7a does not follow this possibility. It is also possible that this reflective ramp, in the middle of the interface, represents the locus of concentrated shear on the subduction thrust itself.

A fourth NW-dipping ramp reflection appears above the ramps of the interface. Note that all these ramps are parallel in the Fig. 7a section to the relocated Weber II aftershocks (Robinson, 1994), distributed along the NW-dipping Weber II thrust-fault plane. This ramp and the ramp at the top of the interface also appear on the S–S reflection and S–P conversion migration images (Fig. 7c and d). We have drawn our

Fig. 7. Individually scaled images of backscattered reflectivity using the Weber II events above the plate interface (a–d) and of mainly forward-scattered reflectivity from Weber I aftershocks below the plate interface (e–h). These images are along the subduction-zone dip section line (Fig. 1). White shows negative reflectivity, black positive reflectivity and gray low reflectivity in these 3-d prestack Kirchhoff migrations of 2–8-Hz bandpass-filtered seismograms. Overlaying the event locations on the sections leads to an interpretable structure for the plate interface. Superimposed are northeastward views into each mainshock's focal sphere and a duplex-thrust interpretation of interface structure. The P–P reflectivity in particular (a, e) is strong and coherently shows the structural details of the plate interface. The upward-curving migration artifacts appear in areas with poor reflection-point coverage and can be ignored. Each of the images, computed for a separate scattered phase, has had its amplitude scaled individually for display. The rms amplitudes of the backscattered P–P (a) and S–S (d) images are similar, the S–P (c) image has about half the amplitude of the P–P reflectivity and the P–S (b) is an order of magnitude lower. The arcing character of the P–S image (b) is due to poor reconstruction of very little P–S energy. The P–P forward scattering (e) is especially strong, considering that an order of magnitude less S–S (h) or P–S (f) forward scattering takes place. The S–P (g) scattering magnitude is about half that of the P–P (e).

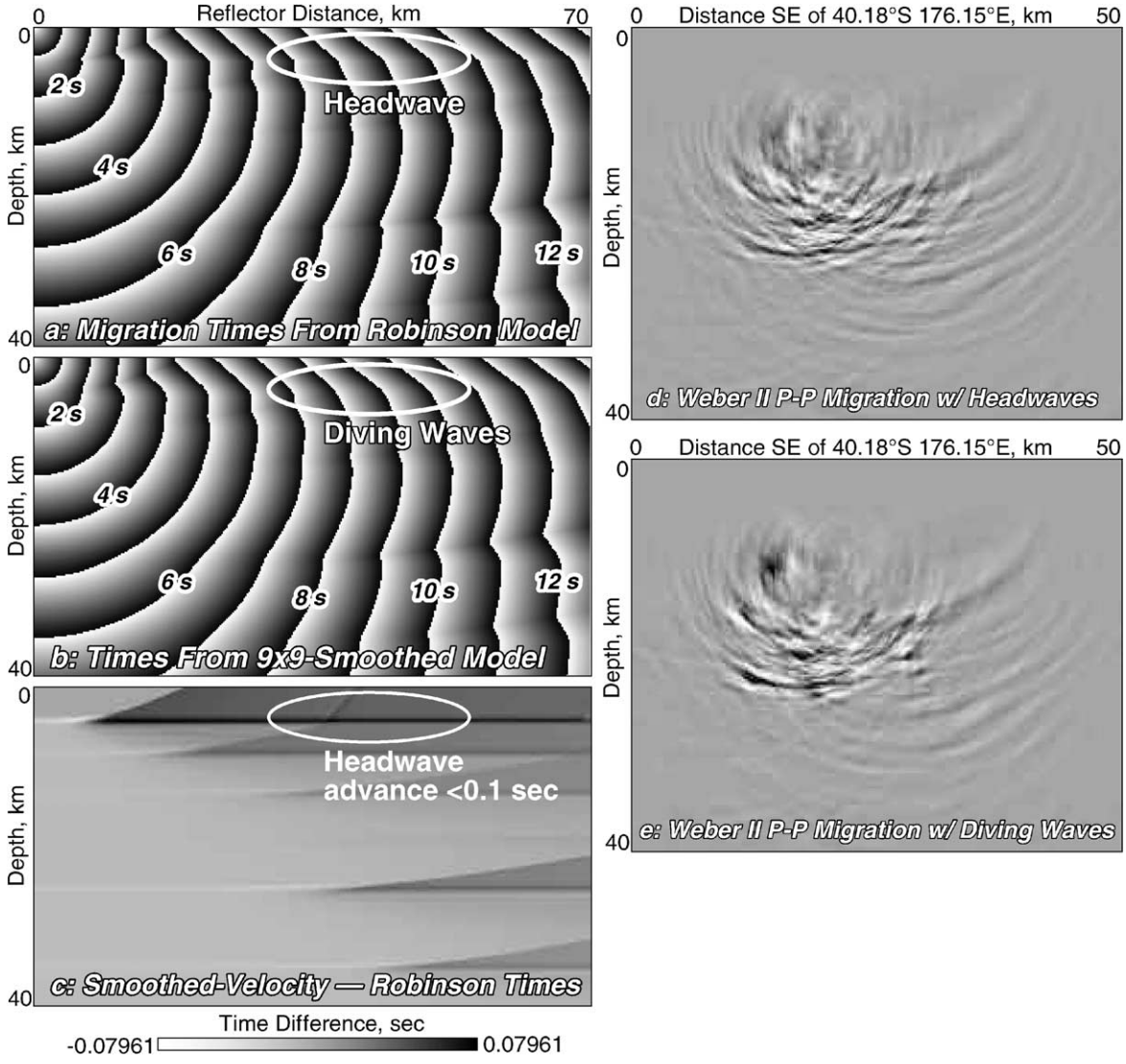

Fig. 8. Test of the effects of migrating possible headwaves. (a) Travel-time section from Robinson's (1994) 1-d velocity model, used in the migrations of Fig. 7, and contoured by taking the time from a source at the upper left, modulo 1 s. (b) The same travel-time section, but computed after smoothing Robinson's velocity model with a 1.8 × 1.8-km 2-d boxcar averaging kernel. Converting the velocity interfaces into gradients removes headwaves and substitutes diving waves, making the angled headwaves (a) into spherical waves (b). (c) Time difference between the smoothed-velocity and the original times. The dark tones show that, just above an interface, a headwave will arrive up to 0.08 s earlier than a diving wave. (d, e) Backscattered P–P migration of Fig. 7a using headwaves, and the same migration employing the smoothed-velocity travel times (Fig. 7b) for imaging. The small difference between (d) and (e) shows the 0.08-s headwave advance of these arrivals to 70-km distance is insignificant in the context of the 2–8-Hz waves migrated.

interpretation to propose that these shingled ramps compose a duplex thrust system, as envisioned for other subduction zones by Karig (1983) and Hashimoto and Kimura (1999). The even spacing of the five shingles, from the top of the Weber I swarm to the Weber II fault, matches the duplexing model. Evidence for the roof thrust can only be seen on the S–S reflection image of Fig. 7d.

The structural interpretation we have drawn on Fig. 7 combines preexisting knowledge of the slab inter-

face with our inferences from synthetic tests and resampled migrations to allow us to identify the backscattered P–P reflections in Fig. 7a that most likely represent real structure. The double-reflector interface is 3–5 km thick and dips 5° NW except where it is offset above the Weber I event by 3–4 km downdip. The frontal ramp of the lower-plate step has raised a thrust duplex (Karig, 1983; Hashimoto and Kimura, 1999) out of the upper 2–3 km of the interface. The frontal ramp of the duplex is visible in the P–P backscattering reflectivity. A previous duplex, aligned with the frontal ramps, could explain the mechanism of the Weber II event. Fault-bend thrusting above the duplex is another possible explanation of that event. The backscattered P–P, S–P, and S–S reflectivity below the Weber I sequence (Fig. 2e,g,h) also suggest a Moho in the Pacific plate at 35-km depth. This Moho depth is suggested by the thickening of the oceanic lower plate throughout the Hikurangi to 15 km total by Chatham Rise plateau basalts or by magmatic underplating (Bannister, 1988; Davey and Stern, 1990).

3.2. Multimode bright spot observations

The forward-scattered images (Fig. 7e–h) suggest strong diffractions on the downdip side of the interface offset. Our images cannot resolve the downdip extent of this "bright spot" of strong scattered amplitude or its exact nature. As shown by the synthetic test in Fig. 6, lack of complete geometric coverage will only present a distorted image of the scattering interface, over just a small part of its total extent. The forward-scattered images take a flame-like shape extending over more than 5-km depth range. The base of the "flame," however, may be close to the true depth of the interface. Scattering of other phases in the data images of Fig. 7e–h seems strongest at the edges of the bright-spot wedge. The forward-scattered images suggest high P-wave scattering potential and low S-wave potential on the downdip side of the Weber I fault's offset.

The strong P–P scattering (both forward and back) without strong P–S, S–P or S–S scattering suggests substantial porosity variations without proportionate rigidity variations. A decrease in P-velocity without a decrease in shear velocity can be achieved by lowering the Poisson's ratio of the material within the slab interface. Oilfield data and porosity–velocity models developed by Pickett (1963) and Castagna et al. (1985) show that shales commonly have Poisson's ratios as low as 0.18. A decrease in Poisson's ratio may also result from a simple increase in pore aspect ratio, from crack-like values below 0.1 to more equant pore shapes with aspect ratios of 0.3–1.0 (Hyndman, 1988).

3.3. Test of headwave effects

Fig. 8 tests the effect of including headwave diffractions in our images. Fig. 8a shows travel time contours from a surface source through Robinson's (1994) velocity model that contains sharp refractors. The diffractive, low-energy headwaves are the straight ramps in the contours. We convert the headwaves to diving waves simply by smoothing away the sharp boundaries in the velocity model. The ramps have become, in Fig. 8b, higher-energy spherical waves.

Dark tones in Fig. 8c show where headwave diffractions would be advanced over diving spherical waves. The maximum advancement is less than 0.1 s, and only appears within 1 km above the refractor. Fig. 8d and e compares a migration imaging condition using diving waves against imaging including diffracted headwaves, for our P–P backscatter data from Fig. 7a. The differences between the images are minimal and do not affect the interpretation. Since we are migrating 2–8-Hz waves, the maximum headwave advance of 0.1 s is immaterial.

3.4. 3-d migrated image volumes

With our Kirchhoff sum imaging technique, true 3-d geometry is always taken into account. Thus, migration into a 3-d image volume, instead of an arbitrarily oriented section, is a simple though time-consuming operation (1–2 h on a Sun Ultra 10, migrating 1739 traces into a 125 × 125 × 200-element image volume). The image volume in Fig. 9 is 25 km on a side and covers a 20-km depth range from 10 to 30-km depth. The oblique slice of the volume in Fig. 9a presents just the central part of the dip section shown in Fig. 7a. It has the same features, as it should, although we have not statistically enhanced the 3-d section and it has more visible artifacts.

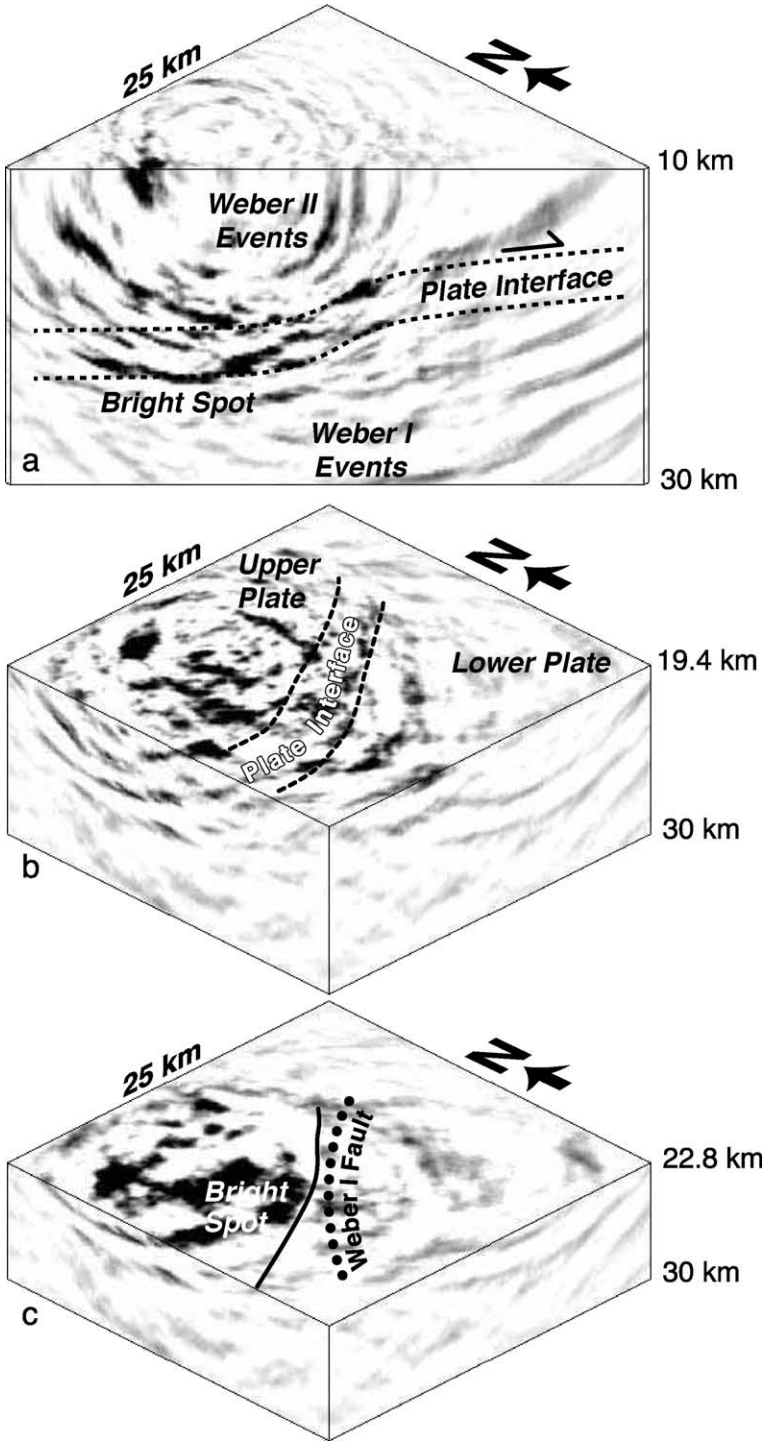
25 km
N
10 km
Weber II
Events
Plate Interface
Bright Spot
Weber I
Events
30 km
a
25 km
N
Upper
Plate
Plate Interface
Lower Plate
19.4 km
30 km
b
25 km
N
Bright
Spot
Weber I Fault
22.8 km
30 km
c

Interpreting the depth slice at 19.4-km depth (Fig. 9b) has the same problems as interpreting a sectional slice. Similar artifacts appear on sections in both directions. The Kirchhoff trajectories of Fig. 5 are approximately ellipsoids of revolution about the sources and receivers at the foci. The artifacts of poor geometric coverage have similar shapes in a constant-depth section to what they show in a cross-section. Resolution of geometric details is limited to areas of the constant-depth section below the sources and receivers, just as it was limited in the cross-sections of Figs. 6 and 7a.

At 20-km depth in Fig. 9b, we can see the 5-km thick plate interface image curving away from the Weber I normal fault (which is deeper) to a more westerly strike. Curvature of the interface seen in the image could be due to artifacts of poor reflection-point coverage. Only the NW half of this depth slice (the left-hand corner) is directly below Weber II events (Fig. 1) and may have sufficient constraint. If the curvature follows a real structure, it is worth noting the close correspondence of this structure with the Weber I normal fault, which is directly below. The plate interface is above the Weber I fault only at its largest total throw in the middle of the volume. The plate interface may be a northwest-plunging synform, with its concave-to-the-northwest shape in the horizontal plan section.

Deeper into the volume on the horizontal section of Fig. 9c, the bright spot of strong P–P reflection (dark tones) at the base of the plate interface appears only west of the Weber I normal fault in the lower plate. Deeper cuts into the volume suggest the high-porosity bright spot is entirely within the plate interface. These 3-d images suggest the bright spot and the duplex-thrusted plate interface are geometrically related. They are both deepest where the preexisting vertical offset of the Weber I normal fault is greatest.

4. Discussion

Our seismic reflectivity images (Figs. 7 and 9) suggest how a subducted normal-fault offset of the sea floor may entrap a thick wedge of reflective sediment. The continental subduction wedge would then be underplated with this sediment through a process of duplex thrusting (Karig, 1983; Hashimoto and Kimura, 1999), effectively accreting oceanic sediment to the bottom of the continental wedge. This process operates where the upper plate is about 20 km thick. Duplexing thickens the plate landward of the thrust stacking (Davey et al., 1986) that extends the very thin upper plate seaward by accretionary outgrowth. Kopp et al. (1999) describe similar accretionary wedge thickening in the Celebes Sea from thickened low-velocity crust.

The frontal ramp of the lower-plate step appears to have raised a duplex thrust out of the upper 2–3 km of the interface. The frontal ramps of the duplexes are visible in the P–P backscattering reflectivity (Fig. 7a). The oldest duplex interpreted on Fig. 7, aligned with the younger frontal ramps underneath and to the SE, could explain the mechanism of the Weber II event. Fault-bend thrusting above the duplex is another possible explanation of that event. Higher topography along the North Island coast (the isolated Puketoi Range, with maximum elevations of 1500 m) above the duplex thrust system is in agreement with this hypothesis. The location of the bright spot of strong scattering appears related to the westward motion of subduction thrusting, and not to the northwest dip of the Weber I fault. This relation suggests tectonic erosion of the accretionary wedge (Ranero and von Huene, 2000) and entrapment of reflective sediment by a few kilometers of preexisting offset on the Weber I normal fault.

Fig. 9. Three-dimensional views of the Weber II backscattered P–P reflectivity volume. The top of the volume is 10 km below the surface, extends to 30-km depth and is 25 km on a side (light box in Fig. 1). Dark tones indicate large-magnitude positive reflectivity; light tones indicate negative or low reflectivity. The views are all toward the northeast along the strike of the subducting slab, which dips down to the left (dashed lines). The top view (a) slices the volume along the NW–SE dip section (Fig. 1) and reproduces the view of the P–P reflectivity seen in Fig. 7a. Because of the distributions of earthquake sources as well as seismograph receivers over regions instead of along lines (Fig. 1), imaging quality within most parts of the volume is just as good as in most parts of this section. The middle view (b) slices the volume horizontally at 19.4-km depth, intersecting the frontal ramps of the interpreted duplex thrust complex, which are most prominent above the trace of the Weber I normal fault. The 3-d image is consistent with the ramps having sunk into the downthrown area of normal offset as a northwest-plunging synform, suggested by the northwest-concave shape (dashed lines) of the structures in horizontal section. The lower view (c) shows that P–P backscattering from the bright spot (Fig. 7) arises in a 10 × 10-km area of the plate interface at 21–23-km depth, west of the Weber I normal fault as defined by Robinson's (1994) aftershock relocations.

Duplex thrusting and wedge thickening by subduction of rugged, normal-faulted oceanic crust was imaged by Ranero and von Huene (2000) along the more steeply dipping subduction zone off Nicaragua. Where Ranero and von Huene (2000) observed seamount subduction, they interpreted erosion and wedge thinning. Reyners et al. (1999), using velocity tomography, saw thickly underplated sediment at 20-km depth pushed in by a high-velocity seamount (as in Kodaira et al., 2000) and interpreted it as accretionary. Our result suggests structural details (Figs. 7 and 9) more consistent with accretion and thickening, but apparently resulting from a subducted normal-fault offset rather than a seamount.

To have the 3–5-km displacement suggested by the migrations, the Weber I normal fault should have been present in the ocean floor at least since its subduction at 3.3 Ma. If it had a significant normal offset before subduction, the fault could have bulldozed a wedge of sediment downdip that has not dewatered as completely as elsewhere in the interface. The fact that we have not observed a significant S–P conversion at the sediment-laden plate interface (Fig. 2) does not agree with the increased Vp/Vs ratio found within the interface by Eberhart-Phillips and Reyners (1999) to the northeast. At Weber, Lamé's lambda parameter must decrease significantly under constant rigidity, lowering the Vp/Vs and Poisson's ratios, to explain our observations. Perhaps up to a 3% increase in porosity, at grain triple junctions but not along intergranular faces, could decrease lambda without decreasing rigidity. Such parameters would be similar to the Cascadia interface modeled by Hyndman (1988), with less lithified and higher-porosity sediments trapped in the plate interface.

5. Conclusions

This natural-source "reflection survey," including forward scattering, was successful in showing active subduction interface geometry at 20-km depth.

1. The Weber I slab-bend normal event is interpreted to maintain a preexisting downdip step in the plate interface. The downdip step might not be a seamount as has been found subducting to the northwest under East Cape.
2. High energy in the P–P forward-scattered image is interpreted as scattering from an anomalous high-porosity wedge of trapped sediment. Porosity is limited to a few percent as bulk rigidity is not much affected.
3. Structural details suggested in the P–P, S–P and S–S backscattered images of the interface are consistent with the Weber II event taking place either on an active duplex thrust, or on a fault-bend thrust above the duplex.
4. The duplex, possibly doubled at the Weber I fault's offset, is consistent with the coastal accretionary wedge topography above. Although the plate interface itself has unknown seismicity, the ramp and the duplex may increase the area's seismic potential.
5. Synthetic tests show that usable backscattered reflectivity images can be obtained from earthquake seismograms recorded on sparse seismometer arrays. Geometric details will be meaningful only directly below a dense swarm of source earthquakes.
6. Images summing forward-scattered energy can show the presence of strong diffractors and mode-conversions, but will not locate them well or show their extent.
7. Computing separate images for P and S reflections as well as mode conversions can yield diagnostic physical property information, most likely related to variations in pore shape and total porosity.

Acknowledgements

Dr. Terry Webb of the New Zealand Crown Institute for Geological and Nuclear Sciences (IGNS) provided access to their comprehensive data base of earthquake seismograms. We thank Russell Robinson of IGNS for providing his earthquake relocations and velocity model. Crucial sabbatical assistance and collaboration were generously provided to J. Louie by E. Smith, M. Savage and J. Taber of the Victoria University of Wellington, New Zealand. S. Chávez-Pérez was partly funded by CONACYT and the Programa de Yacimientos Naturalmente Fracturados at IMP. The kind efforts of two anonymous reviewers helped to substantially improve the manuscript.

References

Aki, K., 1992. Scattering conversions P to S versus S to P. Bull. Seismol. Soc. Am. 82, 1969–1972.

Bannister, S., 1988. Microseismicity and velocity structure in the Hawkes Bay region, New Zealand: fine structure of the subducting Pacific plate. Geophys. J. 95, 45–62.

Castagna, J.P., Batzle, M.L., Eastwood, R.L., 1985. Relationships between compressional-wave and shear-wave velocities in clastic silicate rocks. Geophysics 50, 571–581.

Chávez-Pérez, S., Louie, J.N., 1998. Crustal imaging in southern California using earthquake sequences. Tectonophysics 286, 223–236.

Chávez-Pérez, S., Louie, J.N., Pullammanappallil, S.K., 1998. Seismic depth imaging of normal faulting in the southern Death Valley basin. Geophysics 63, 223–230.

Davey, F.J., Smith, E.G.C., 1983. A crustal seismic reflection–refraction experiment across the subducted Pacific Plate under Wellington, New Zealand. Phys. Earth Planet. Inter. 31, 327–333.

Davey, F.J., Stern, T.A., 1990. Crustal seismic observations across the convergent plate boundary, North Island, New Zealand. Tectonophysics 173, 283–296.

Davey, F.J., Hampton, M., Childs, J., Fisher, M.A., Lewis, K., Pettinga, J.R., 1986. Structure of a growing accretionary prism, Hikurangi margin, New Zealand. Geology 14, 663–666.

Davey, F.J., Henrys, S., Lodolo, E., 1997. A seismic crustal section across the East Cape convergent margin, New Zealand. Tectonophysics 269, 199–215.

DeMets, C., Gordon, R.G., Argus, D.F., Stein, S., 1994. Effect of recent revisions to the geomagnetic reversal time scale on estimates of current plate motions. Geophys. Res. Lett. 21, 2191–2194.

Eberhart-Phillips, D., Reyners, M., 1999. Plate interface properties in the northeast Hikurangi subduction zone, New Zealand, from converted seismic waves. Geophys. Res. Lett. 26, 2565–2568.

Flueh, E.R., Fisher, M.A., Bialas, J., Childs, J.R., Klaeschen, D., Kukowski, N., Parsons, T., Scholl, D.W., ten Brink, U., Trehu, A.M., Vidal, N., 1998. New seismic images of the Cascadia subduction zone from cruise SO108-ORWELL. Tectonophysics 293, 69–84.

Hale, D., Claerbout, J.F., 1983. Butterworth dip filters. Geophysics 48, 1033–1038.

Harlan, W.S., Claerbout, J.F., Rocca, F., 1984. Signal/noise separation and velocity estimation. Geophysics 49, 1869–1880.

Hashimoto, Y., Kimura, G., 1999. Underplating processes from melange formation to duplexing: example from the Cretaceous Shimanto Belt, Kii Peninsula, Southwest Japan. Tectonics 18, 92–107.

Hu, L.-Z., McMechan, G.A., Harris, J.M., 1988. Acoustic prestack migration of cross-hole data. Geophysics 53, 1015–1023.

Hyndman, R.D., 1988. Dipping seismic reflectors, electrically conductive zones, and trapped water in the crust over a subducting plate. J. Geophys. Res. 93, 13391–13405.

Igel, H., Ben-Zion, Y., Leary, P.C., 1997. Simulation of SH- and P–SV-wave propagation in fault zones. Geophys. J. Int. 128, 533–546.

Ikelle, L.T., Kitchenside, P.W., Schultz, P.S., 1992. Parametrization of GRT inversion for acoustic and P–P scattering. Geophys. Prospect. 40, 71–84.

Karig, D.E., 1983. Accreted terranes in the northern part of the Philippine Archipelago. Tectonics 2, 211–236.

Kodaira, S., Takahashi, N., Nakanishi, A., Miura, S., Kaneda, Y., 2000. Subducted seamount imaged in the rupture zone of the 1946 Nankaido earthquake. Science 289, 104–106.

Kopp, C., Flueh, E.R., Neben, S., 1999. Rupture and accretion of the Celebes Sea crust related to the North-Sulawesi subduction: combined interpretation of reflection and refraction seismic measurements. J. Geodyn. 27, 309–325.

Le Bras, R., 1985. Methods of multiparameter inversion of seismic data using the acoustic and elastic Born approximations. PhD thesis, California Institute of Technology, 141 pp.

Le Bras, R.J., Clayton, R.W., 1988. An iterative inversion of back-scattered acoustic waves. Geophysics 53, 501–508.

Levander, A.R., 1988. Fourth-order finite-difference P–SV seismograms. Geophysics 53, 1425–1436.

Louie, J.N., 1990. Physical properties of deep crustal reflectors in southern California from multioffset amplitude analysis. Geophysics 55, 670–681.

Louie, J.N., Clayton, R.W., Le Bras, R.J., 1988. Three-dimensional imaging of steeply dipping structure near the San Andreas fault, Parkfield, California. Geophysics 53, 176–185.

Lumley, D.E., Claerbout, J.F., Bevc, D., 1994. Anti-aliased Kirchhoff 3-D migration. 64th Annual International Meeting, Expanded Abstracts, Soc. Expl. Geophys., Tulsa, OK, pp. 1282–1285.

Mittet, R., Hokstad, K., Helgesen, J., Canadas, G., 1997. Imaging of offset VSP data with an elastic iterative migration scheme. Geophys. Prospect. 45, 247–267.

Pickett, G.R., 1963. Acoustic character logs and their applications in formation evaluation. J. Pet. Technol. 15, 650–667.

Ranero, C.R., von Huene, R., 2000. Subduction erosion along the Middle America convergent margin. Nature 404, 748–752.

Reyners, M.E., 1980. A microearthquake study of the plate boundary, North Island, New Zealand. Geophys. J. R. Astron. Soc. 63, 1–22.

Reyners, M., Eberhart-Phillips, D., Stuart, G., 1999. A three-dimensional image of shallow subduction: crustal structure of the Raukumara Peninsula, New Zealand. Geophys. J. Int. 137, 873–890.

Robinson, R., 1986. Seismicity, structure and tectonics of the Wellington region, New Zealand. Geophys. J. R. Astron. Soc. 87, 379.

Robinson, R., 1994. Shallow subduction tectonics and fault interaction: the Weber, New Zealand, earthquake sequence of 1990–1992. J. Geophys. Res. 99, 9663–9679.

Sato, H., 1984. Attenuation and envelope formation of three-component seismograms of small local earthquakes in randomly inhomogeneous lithosphere. J. Geophys. Res. 89, 1221–1241.

Tan, T.H., 1985. The elastodynamic field of N interacting vibrators (two-dimensional theory). Geophysics 50, 1229–1252.

Vidale, J.E., 1988. Finite-difference calculation of travel times. Bull. Seismol. Soc. Am. 78, 2062–2076.

Von Seggern, D., 1994. Depth imaging resolution of 3-D seismic recording patterns. Geophysics 59, 564–576.

Wu, R.-S., Aki, K., 1985. Scattering characteristics of elastic waves by an elastic heterogeneity. Geophysics 50, 582–595.

Zhiming, L., Ottolini, R., Claerbout, J.F., 1984. Migrating reflections greater than 90 degrees via depth extrapolation. 54th Annual International Meeting, Soc. Explor. Geophys., Expanded Abstracts, 696–700.

Zhu, J., Lines, L., 1997. Reverse-time migration of sparse and irregular data. J. Seismic Explor. 6, 45–58.